INTERNATIONAL JOURNAL FOR NUMERICAL METHODS IN FLUIDS
Int. J. Numer. Meth. Fluids 2000; **33**: 993–1026

Computation of free surface flows with a Taylor–Galerkin/pressure–correction algorithm

V. Ngamaramvaranggul and M. F. Webster*

Institute of Non-Newtonian Fluid Mechanics, Department of Computer Science, University of Wales, Swansea, U.K.

SUMMARY

A semi-implicit Taylor–Galerkin/pressure–correction finite element scheme (STGFEM) is developed for problems that manifest free surfaces associated with the incompressible creeping flow of Newtonian fluids. Such problems include stick–slip and die-swell flows, both with and without a superimposed drag flow, and for plane, axisymmetric and annular systems. The numerical solutions are compared with available analytical and numerical solutions, both in the neighbourhood of singularities and elsewhere. Close correspondence in accuracy is extracted from the literature for both stick–slip and die-swell flows. Stick–slip flow is used as a precursor study to the more complex free surface calculations involved for die-swell in extrudate flow. Two different free surface techniques are reported and results are analysed with mesh refinement and varying structure. Copyright © 2000 John Wiley & Sons, Ltd.

KEY WORDS: annular flow; die swell; finite element method; Poiseuille flow; pressure–correction; stick–slip; Taylor–Galerkin; time stepping scheme

1. INTRODUCTION

The focus of this paper is the investigation of a finite element time stepping scheme based on pressure–correction in its application to free surface flows for Newtonian fluids. Intrinsic to this study is the implementation of free surface location techniques. The numerical method is based upon a semi-implicit Taylor–Galerkin/pressure–correction finite element method (STGFEM) [1,2], which has been successfully implemented in a variety of different flow circumstances. Specific problems considered are stick–slip and die-swell flows under creeping conditions. These flows are analysed in two-dimensional plane, axisymmetric and annular co-ordinate systems. Annular flows are taken as pressure-driven with a superimposed drag flow, chosen as characteristic case studies relevant to the industrial process of wire-coating.

For stick–slip flow, comparison is made against the analytical solution of Richardson [3] for plane creeping flow. Many problems described via systems of partial differential equations, display singular solutions near corners or crack tips. The region between stick and slip

* Correspondence to: Institute of Non-Newtonian Fluid Mechanics, Department of Computer Science, University of Wales, Swansea, Singleton Park, Swansea SA2 8PP, U.K.

Received March 1999
Revised September 1999

manifests just such a singularity. The flow behaviour in the neighbourhood of such singular points is of particular interest, where high stress concentration or sharp velocity gradients prevail. This influences the solution locally and demands a high concentration of low-order elements for adequate representation. To reduce this effect, Okabe [4] presented the theory of semi-radial singularity mapping, which provides for stress and strain near the singularity with bounded strain energy. Following the solution of Richardson, various numerical methods were introduced to improve accuracy. Ingham and Kelmanson [5] estimated the solution in the neighbourhood of the singularity and accelerated the rate of convergence using a singular boundary element method (SBEM). Kermode *et al.* [6] calculated the solution near a singular point using a finite element method (FEM) [7] and a least-squares fitting procedure. They retained the first three terms of the singular expansion series. Georgiou *et al.* [8] improved the solution accuracy over continuous methods in the neighbourhood of the singular point using a singular finite element method (SFEM). In a subsequent study, Georgiou *et al.* [9] further developed the integrated singular basis function method (ISBFM) in application to stick–slip and die-swell flows. These singular function methods provide a sound basis for comparison of the quality of solutions generated by the present methodology, above and beyond that of Richardson.

Extrudate flow from a die is a special case of a stick–slip flow, where the free surface shape itself must be estimated. This is an important issue in rheology and has considerable significance to polymer processing operations in industry. Richardson [3] also supplied an analytical solution for this case with integral transforms, for large surface tension under creeping flow conditions and without gravitational effects. Tanner [10] has provided data from the literature on the use of several numerical schemes to compute die-swell flow, e.g. finite element, finite difference and boundary element, and comments on the better performing algorithms to estimate the position of the free surface streamline. Tanner catalogues results for swelling ratio covering axisymmetric and planar dies for Newtonian and viscoelastic flows. An asymptotic result is also quoted [10] as a simple approach for estimating practical extrudate swell calculations, where the surface tension of the extrudate is not a dominant factor.

A number of authors have employed FEM techniques for creeping die-swell flow. Using a classical FEM implementation with fine meshing, Nickell *et al.* [11] demonstrated solutions for viscous incompressible jet and free surface flows of Newtonian fluids. Chang *et al.* [12] studied die-swell for Newtonian and viscoelastic fluids by Galerkin and collocation methods. Crochet and Keunings [13] dealt with slit, circular and annular dies for Newtonian and Maxwell fluids, introducing a mixed FEM. Crochet and Keunings [14] went further to show that mesh refinement, with increased concentration of elements at the singularity, has a major impact on die-swell calculations. We cite Silliman and Scriven [15] for their work on free surface treatment for Newtonian fluids, though their principal focus was concerned with slip (see our companion study [16]) and surface tension effects on free surface shape. Phan-Thien [17] also considered slip effects with a boundary element method (BEM), in planar flows for viscoelastic fluids. This study is relevant for the proposed alternative free surface location technique therein. Beverly and Tanner [18] used boundary and finite element methods to consider extrusion of Newtonian fluids at finite Reynolds number for planar, axisymmetric and three-dimensional dies. They found that in an unconstrained extrudate, the particles in the free extrudate will follow spirals or helices. In passing, we point out that thermal effects have also been found to influence free surface shape [19].

Beyond the consideration of numerical solutions, some experimental results are presented in Butler and Bush [20] and Ahmed *et al*. [21]. Butler and Bush provided experimental evidence for dilute viscoelastic fluids (polyisobutylene–polybutene) in axisymmetric isothermal flows. Ahmed *et al*. found correspondence between experimental observations and the numerical solutions derived from an FEM in planar entry flows and die-swell flows for molten polyethylenes.

Our interests lie in the generalization of the STGFEM to incorporate the treatment of free surfaces and, in particular, in applications for non-Newtonian flows. In the case of planar stick–slip flow, the STGFEM approach is shown to provide accurate numerical results as compared with analytical solutions for velocity and pressure. Close correspondence is extracted for our numerical solutions near the singularity with those of the literature. The influence of die-swell is established in contrast to stick–slip flow. We are able to quantify the difference that drag flow has on stick–slip flow via the change in pressure drop, peak shear rates and adjustment in free-stream velocity. Likewise, we are able to draw on comparison between die-swell and die-swell/drag flow, to indicate the reduction in swelling ratio and angle and peak shear rates. In addition, this paper provides a useful pilot study for the analysis of annular pressure-driven drag flows, typical of those that arise in tube- or pressure-tooling settings for wire-coating.

2. GOVERNING EQUATIONS

For Newtonian fluids and incompressible isothermal flow in the absence of body forces, the governing equations are those of generalized momentum and continuity, which may be expressed as

$$\rho \mathbf{U}_t = \nabla\cdot(\mu\nabla\mathbf{U}) - \rho\mathbf{U}\cdot\nabla\mathbf{U} - \nabla p \tag{1a}$$

$$\nabla\cdot\mathbf{U} = 0 \tag{1b}$$

where variables velocity ($\mathbf{U}$) and pressure (p) are defined over space and time with temporal derivative represented as $\mathbf{U}_t$. Material parameters are given via density (ρ) and viscosity (μ).

For constant μ, the celebrated Navier–Stokes equations emerge. To non-dimensionlize, we select the following characteristic scales: length L, velocity V, time L/V, pressure $\mu_0 V/L$. We may define the following dimensionless variables and differential operators:

$$U^* = \frac{1}{V}U, \qquad p^* = \frac{L}{\mu_0 V}p, \qquad t^* = \frac{V}{L}t$$

$$Z^* = \frac{1}{L}Z, \qquad r^* = \frac{1}{L}r, \qquad \mu^* = \frac{1}{\mu_0}\mu$$

$$\nabla^* = L\nabla, \qquad \frac{\mathrm{D}}{\mathrm{D}t^*} = \frac{L}{V}\frac{\mathrm{D}}{\mathrm{D}t}$$

where μ_0 is a reference viscosity.

Substitution of the above dimensionless variables and differential operators into Equation (1) yields the non-dimensional generalized Navies–Stokes equations, which may be started in the following form:

$$Re\,\mathbf{U}_t = \nabla\cdot(\nabla\mathbf{U}) - Re\,\mathbf{U}\cdot\nabla\mathbf{U} - \nabla p \tag{2a}$$

$$\nabla\cdot\mathbf{U} = 0 \tag{2b}$$

where $Re = \rho LV/\mu_0$ is the non-dimensional group number termed the Reynolds number.

3. NUMERICAL SCHEME

3.1. Discretization

To solve the Navier–Stokes equation (2a), together with the incompressibility constraints (2b), we employ a semi-implicit time stepping procedure, namely a Taylor–Galerkin/pressure–correction finite element scheme [1] as cited above. Briefly, the Taylor–Glerkin-based algorithm is a fractional step method that semi-discretizes first in the temporal domain using Taylor series expansions in time and a pressure–correction procedure, to extract a time stepping scheme of second-order accuracy. The discretization is completed via a spatial Galerkin FEM. We assume that the flow domain is discretized into a triangular mesh, and that piecewise continuous linear (pressure) and quadratic (velocity) interpolation functions apply on such elemental regions. The Taylor–Galerkin algorithm has three distinct fractional stages per time step as follows.

Stage 1
Given initial velocity and pressure fields, non-divergence-free $u^{n+1/2}$ and u^* fields are calculated via a two-step predictor–corrector procedure. The corresponding mass matrix governed equations are solved iteratively by a Jacobi method.

Stage 2
Using u^*, calculate the pressure difference $(p^{n+1} - p^n)$ via a Poisson equation, applying a Choleski method of solution.

Stage 3
Using u^* and the pressure difference $(p^{n+1} - p^n)$, determine a divergence-free velocity field u^{n+1} by Jacobi iteration.

Adopting quadratic and linear interpolations, $\mathbf{U}(\mathbf{x}, t)$ and $\mathbf{P}(\mathbf{x}, t)$, to the solution, where

$$\mathbf{U}(\mathbf{x}, t) = U_j(t)\Phi_j(\mathbf{x}), \qquad \mathbf{P}(\mathbf{x}, t) = P_j(t)\psi_j(\mathbf{x})$$

we may proceed to solve Equations (2a) and (2b). The fully discrete formulation STGFEM over a single time step, $\Delta t = t^{n+1} - t^n$, may be represented in the following matrix–vector notation:

Stage 1a

$$\left(\frac{2Re}{\Delta t}\,\mathbf{M}+\frac{1}{2}\mathbf{S}_u\right)(\mathbf{U}^{n+1/2}-\mathbf{U}^n)=\{-[\mathbf{S}_u\mathbf{U}+Re\mathbf{N}(\mathbf{U})\mathbf{U}]+\mathbf{L}^T\mathbf{P}\}^n$$

Stage 1b

$$\left(\frac{2Re}{\Delta t}\,\mathbf{M}+\frac{1}{2}\,\mathbf{S}_u\right)(\mathbf{U}^*-\mathbf{U}^n)=[-\mathbf{S}_u\mathbf{U}+\mathbf{L}^T\mathbf{P}]^n-Re[\mathbf{N}(\mathbf{U})\mathbf{U}]^{n+1/2}$$

Stage 2

$$\mathbf{K}(\mathbf{P}^{n+1}-\mathbf{P}^n)=-\frac{2}{\Delta t}\,\mathbf{L}\mathbf{U}^*$$

Stage 3

$$\frac{Re}{\Delta t}\,\mathbf{M}(\mathbf{U}^{n+1}-\mathbf{U}^*)=\frac{1}{2}\,\mathbf{L}^T(\mathbf{P}^{n+1}-\mathbf{P}^n)$$

where variables are defined as nodal vectors at time t^n for velocity ($\mathbf{U}^n$) and pressure ($\mathbf{P}^n$), an intermediate non-solenoidal nodal velocity vector ($\mathbf{U}^*$), mass matrix ($\mathbf{M}$), momentum diffusion matrix ($\mathbf{S}_u$), a pressure stiffness matrix ($\mathbf{K}$), convection matrix [$\mathbf{N}(\mathbf{U})$] and divergence/pressure gradient matrix ($\mathbf{L}$).

In matrix notation, we have

$$\mathbf{M}_{ij}=\int_\Omega r\phi_i\phi_j\,\mathrm{d}\Omega$$

$$\mathbf{K}_{ij}=\int_\Omega r(\nabla\psi_i\cdot\nabla\psi_j)\,\mathrm{d}\Omega$$

$$\mathbf{N}(\mathbf{U})_{ij}=\int_\Omega r\phi_i\left(U_k^l\phi_l\frac{\partial\phi_j}{\partial x_k}\right)\mathrm{d}\Omega$$

$$(\mathbf{L}_k)_{ij}=\int_\Omega r\phi_i\frac{\partial\phi_j}{\partial x_k}\,\mathrm{d}\Omega$$

$$(\mathbf{S}_u)_{ij}=(\mathbf{S}_{lm}+\mathbf{V}_{lm})_{ij}$$

$$(\mathbf{S}_{lm})_{ij}=\int_\Omega r\mu\left(\chi_{lk}\frac{\partial\phi_i}{\partial x_k}\frac{\partial\phi_j}{\partial x_k}\right)\mathrm{d}\Omega,\quad \text{if } l=m$$

$$(\mathbf{S}_{lm})_{ij} = \int_{\Omega} r\mu \left(\frac{\partial \phi_i}{\partial x_m} \frac{\partial \phi_j}{\partial x_l} \right) \mathrm{d}\Omega, \quad \text{if } l \neq m$$

where $k, l = 1, 2$; $x_1 = r$, $x_2 = z$; $\chi_{lk} = 2$ if $l = k$ and $\chi_{lk} = 1$ if $l \neq k$; and

$$(\mathbf{V}_{lm})_{ij} = \frac{2\phi_i \phi_j}{r^2} \quad \text{if } l = m = 1$$

$$(\mathbf{V}_{lm})_{ij} = 0 \quad \text{if } l, m \neq 1$$

The time stepping procedure is monitored for convergence to a steady state via relative increment norms (using both maximum and least-squares measures) subject to satisfaction of a suitable tolerance criteria, here taken as 10^{-5}.

3.2. Free surface location

The extent of extrudate swell in a die-swell flow may be determined by implementing a free surface location method via a modified iterative technique (e.g. in industrial casting processes). According to Crochet *et al.* [22], the following three boundary conditions may be defined on a free surface:

$$v_r n_r + v_z n_z = 0 \tag{3}$$

$$t_r n_r + t_z n_z = S\left(\frac{1}{\rho_1} + \frac{1}{\rho_2} \right) \tag{4}$$

$$t_r n_z - t_z n_r = 0 \tag{5}$$

with variables specification of radial velocity (v_r), axial velocity (v_z), components of the unit normal to the free surface (n_r, n_z), surface force normal to the surface (t_r, t_z), principal radii of curvature (ρ_1, ρ_2) and surface tension coefficient (S).

Typically, when modelling a free surface iteratively, conditions (4) and (5) are enforced as boundary conditions. Then the normal velocity is calculated using Equation (3) and this is used to describe the shape of the upper extrudate boundary for say die-swell flow, as illustrated in Figure 1(c). In the free jet flow, the distance from the axis of symmetry is

$$r(z) = R + \int_{z=0}^{\infty} \mathrm{d}z \, \frac{v_r(z)}{v_z(z)} \tag{6}$$

where R is the tube radius.

In this paper, the integral in Equation (6) is evaluated by Simpsons quadrature rule, thus providing an estimate of the extrudate shape. The comparison of Richardson's [3] asymptotic results for swell ratio ($\chi = R_j/R$, R_j is jet radius, R is tube radius) with those from a finite element calculation is catalogued in Silliman and Scriven [15]. Phan-Thien [17] focuses on the extrudate shape as it varies due to slip at the wall and compares the swelling ratio for various

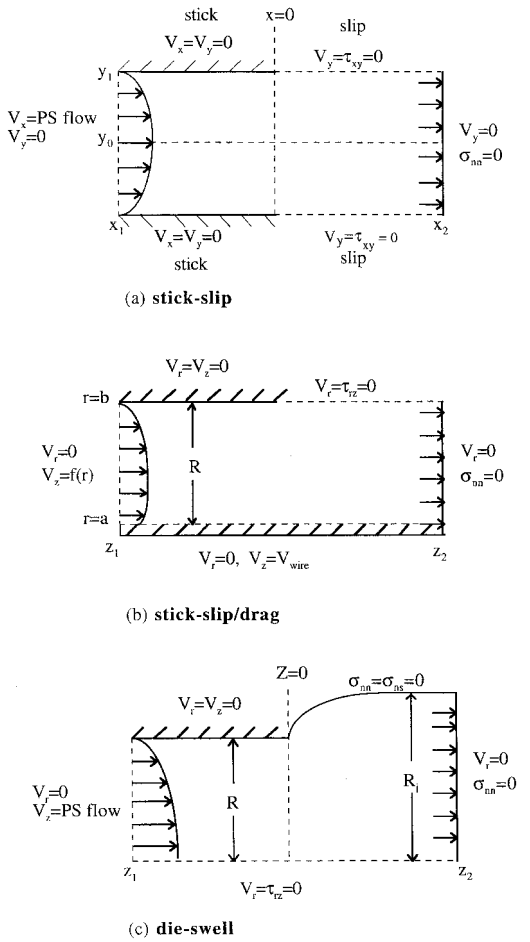

Figure 1. Schema for flow problems.

critical wall shear stresses, employing an alternative free surface updating strategy. The implementation of the process is straightforward. First, the free surface must be estimated from a pervious solution. The function describing any free surface at time t is defined as $\mathbf{h} = \mathbf{h}(z, t)$ so that at the free surface the following equation holds and must be updated at each time step:

$$\frac{\partial \mathbf{h}}{\partial t} = v_r - v_z\left(\frac{\partial \mathbf{h}}{\partial z}\right) = G(\mathbf{U}(t), \mathbf{h}(t)) \tag{7}$$

where $\mathbf{U} = (v_r, v_z)$. The free surface equation (7) is updated in time by either a first- or second-order scheme. Considered in a pointwise manner in space, the first-order Euler scheme with chosen time step Δt, is provided by

$$\mathbf{h}(z, t+\Delta t) = \mathbf{h}(z, t) + \Delta t\, G(\mathbf{U}(t), \mathbf{h}(z, t))$$

To derive a second-order scheme, the temporal series is pursued to higher-order terms

$$\mathbf{h}(z, t+\Delta t) = \mathbf{h}(z, t) + \Delta t\, G(\mathbf{U}(t), \mathbf{h}(z, t)) + \frac{1}{2}(\Delta t)^2 \frac{\partial}{\partial t} G(\mathbf{U}(t), \mathbf{h}(z, t))$$

An alternative second-order scheme is a two-step implementation due to Heun

$$\mathbf{h}' = \mathbf{h}(z, t) + \Delta t\, G(\mathbf{U}(t), \mathbf{h}(z, t))$$

$$\mathbf{h}(z, t+\Delta t) = \mathbf{h}(z, t) + \frac{1}{2}(\Delta t)[G(\mathbf{U}(t), \mathbf{h}(z, t)) + G(\mathbf{U}(t), \mathbf{h}'(z, t))]$$

The results from the implementation of Euler and Heun schemes prove remarkably similar, and therefore only those for the Euler scheme are discussed in this article.

4. PROBLEM SPECIFICATION

There are essentially two types of problems studied here, stick–slip flow and die-swell flow. A variant within each category is to consider, in addition, a drag flow component. Poiseuille stick–slip flow is taken within a Cartesian framework and also under an annular configuration when drag flow is imposed simultaneously. For the case of Poiseuille die-swell, the benchmark axisymmetric setting is taken first, this being followed by an annular instance with drag-flow. A visual schemata of the boundary conditions for the stick–slip flow, stick–slip/drag flow and die-swell flow are given in Figure 1. Velocity conditions are imposed as essential conditions, while stress conditions arise naturally in weak form (see Silliman and Scriven [15]). Initial conditions for this time stepping scheme are taken as either quiescent for stick–slip instances, or for die swell flows, from a precomputed steady state solution with an estimated free surface location.

4.1. Planar stick–slip flow

The stick–slip flow problem consists of two regions with distinct boundary conditions, a channel section and a free jet flow section. Considering the planar case, stick or no-slip boundary conditions apply at the channel walls, to adjust subsequently to slip boundary conditions beyond the channel, as shown in Figure 1(a). This implies that tangential velocity and shear stress vanish on the free surface, as does cross-stream velocity and normal stress (Cauchy stress defined as σ) at the outlet.

We use the notation PS to imply Poiseuille flow as given by a one-dimensional velocity profile of the dimensionless form $V_x(y) = V_{\max}(1-y^2)$, with maximum inlet velocity $V_{\max}$. Characteristic scales of length and velocity are adopted as half channel width and average inlet velocity respectively. This problem is solved using the STGFEM above on three uniform and

one biased mesh; the details of which are specified in Table I and illustrated in Figure 2. The smallest element in the biased case is located adjacent to the singularity. Comparison of the results obtained is made against those of Richardson [3] and Nickell *et al.* [11] in Section 5.1. To this end, the implementation is considered for creeping flow in the upper half plane through symmetry. A vanishing pressure datum is set on the top slip surface and outer boundary. Dimensionless quantities are taken as $x_1 = -2$, $x_2 = 2$, $y_0 = 0$, $y_1 = 1$ and $V_{\max} = 1.5$ units.

4.2. Axisymmetric stick–slip flow (ASSF)

The boundary conditions for the axisymmetric case of stick–slip flow are similar to those for the planar stick–slip flow described in Section 4.1, Figure 1(a). The only difference in the governing conditions lies in the introduction of a cylindrical co-ordinate system. A Poiseuille flow is imposed at the inlet. Advantage may be taken of symmetry radially, so that solutions are sought in the top half plane, noting that this implies a lower symmetry boundary where the radial velocity vanishes. Characteristic scales of length and velocity are taken as channel width and maximum inlet velocity. Dimensionless quantities are channel radius and length of unity, jet length of two. Henceforth, for all flows considered a finite small value of the Reynolds number is assumed to emulate practical creeping conditions, $Re = 10^{-4}$. For this case, we have generated a biased fine mesh for adequate resolution, which is finer than that employed for the planar counterpart problem, with elements 18×54, nodes 4033, and size of element 2.6083×10^{-2}, as demonstrated in Figure 8(a).

4.3. Stick–slip/drag flow (SSDF)

This is a more complex annular flow configuration than conventional axisymmetric stick–slip flow for which the mesh of Figure 8(a) is employed, Such a problem instance is initiated from an inlet annular pressure-driven base flow with a superimposed drag flow on the inner boundary. Remaining boundary conditions follow stick–slip flow as cited above. A schematic illustration is provided with boundary conditions in Figure 1(b). The velocity v_z at the inlet is defined by Equation (A.1) of Appendix A. Such a specification may be found in wire-coating, for example, where the inner boundary represents a wire moving at a constant speed taken here of non-dimensional radial dimension $a = 0.15$ units. Characteristic scales are taken for length as inlet hydraulic radius R and for velocity as in Section 4.2 for axisymmetric stick–slip flow. This leads to equivalent flow rates in both flow settings. Dimensionless quantities result as $z_1 = -1$, $z_2 = 2$, jet length of 2, wire speed $V_{\text{wire}} = 0.5$, and $b = 1.15$ units.

Table I. Finite element meshes for stick–slip flow.

Mesh	Element	Total element	Size of element (Δh)
(a) Coarse mesh	5×20	200	0.200
(b) Medium mesh	10×40	800	0.100
(c) Fine mesh	15×60	1800	0.067
(d) Biased fine mesh	15×60	1800	0.024

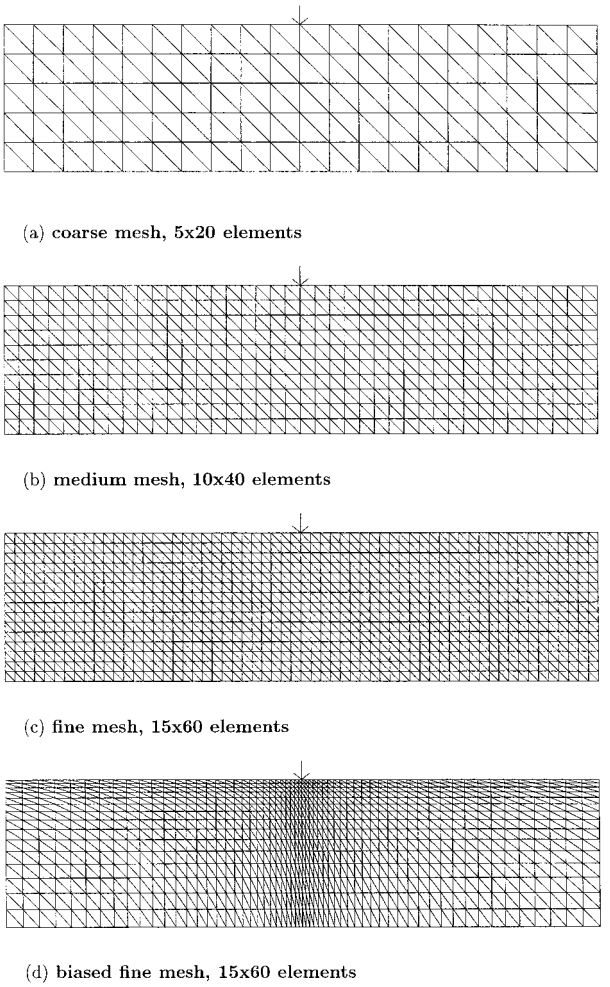

Figure 2. Planar stick–slip flow: mesh patterns.

4.4. Die-swell flow

The die swell problem may be identified via two regions of different character, the shear flow within the die and the free jet flow beyond it. Each region has its unique set of boundary conditions and the problem is posed in an axisymmetric frame of reference. Poiseuille flow is imposed at the inlet. The outer wall boundary experiences stick conditions in the die section, changing to slip conditions at the free meniscus surface beyond the die. Channel radius and maximum inlet velocity are taken as characteristic scales, following Section 4.2. A schematic representation of the problem is presented in Figure 1(c), with notation for Cauchy stress (σ), unit normal vector (n) and unit tangential vector (s) to the respective surface.

Under the assumption of negligible surface tension die-swell flow is simulated for a range of refined meshes, coarse, medium and fine, with two different mesh structures. This permits an analysis of consistency, order of accuracy and provides insight as to the influence of mesh structure on the solution. The meshing details are given in Figure 10, where Δh is a measure of the smallest size of element.

4.5. Die-swell/drag flow

This problem is a combination of those stated previously taking the drag flow described under stick–slip with the die-swell specification. The free surface conditions remain unchanged, and the inner boundary (wire) moves at a constant speed of 0.5 units. The same characteristic scales of length and velocity, and dimensionless quantities of Section 4.3 are adopted in this case. The inlet profile is determined from Equation (A.1) of Appendix A. This problem is simulated on the same three levels of mesh refinement as for the die-swell problem, where we have pre-selected the better performing mesh option with UD structure, see Table II, Figure 10 and comments below.

5. RESULTS AND DISCUSSION

5.1. Planar stick–slip flow

First the coarse, medium and fine meshes of Table I and Figure 2 are considered. The location of the stick–slip singularity is indicated by arrow in Figure 2. On the medium mesh the velocity vector plot of Figure 3(a) illustrates the general pattern of the flow for the upper half plane, that is visually identical for meshes (a), (b) and (c) of Table I. This shows an initial Poiseuille flow that gradually adjusts to a plug flow. Figure 3(b) and (c) represents the horizontal (V_x) and vertical (V_y) velocity component line contours. Figure 3(b) shows V_x with no-slip at the upper boundary to channel exit, whereupon V_x gradually increases, becoming faster with increasing distance along the top surface (reflecting slip conditions). The vertical velocity (V_y) line plot of Figure 3(c) vanishes at inlet and outlet, top surface and symmetry axis, and displays closed contours of constant value in the neighbourhood of the singularity, see Nickell [11]. The centre of the plot demonstrates a peak maximum value of 0.17 units.

Table II. Finite element meshes for die-swell flow.

Mesh	Element	Total element	Direction	$\Delta h * 10^{-2}$
(a) Coarse UD mesh	6×18	216	◣	6.4550
(b) Medium UD mesh	12×36	864	◣	3.0533
(c) Fine UD mesh	18×54	1944	◣	1.9667
(d) Coarse DU mesh	6×18	216	◢	6.4550
(e) Medium DU mesh	12×36	864	◢	3.0533
(f) Fine DU mesh	18×54	1944	◢	1.9667

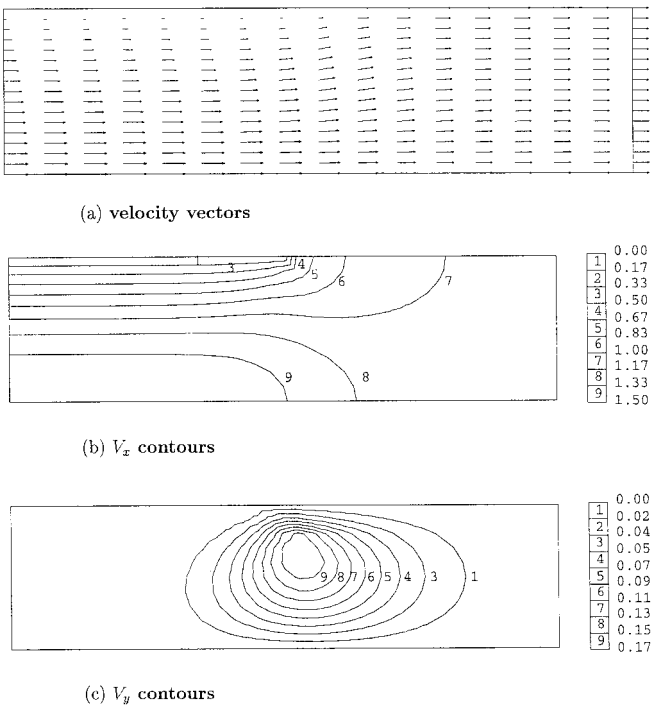

Figure 3. Velocity results for planar stick–slip flow: medium mesh, $Re = 0$.

The shear rate I_2 contour plot (Figure 4(b) representing the second invariant of the rate of strain tensor) demonstrates the formation of a singularity at the die exit, which is again represented clearly in the line plot of Figure 4(c). The shear rate at the top surface (Figure 4(c)) increases exponentially towards the die exit ($x = 0$) to a maximum of 8.28 units. On moving away from the die, a sharp drop is displayed with shear rate tending to zero at $x = 2$ units. Figure 4(a) shows a contour plot of pressure for this problem. A maximum value in pressure is observed of 6.89 units at the inlet boundary, which represents the pressure drop across the flow, a minimum pressure of -2.79 units occurs near the singularity.

Table III gives the comparison of maximum shear rate I_2, which occurs at the top free surface, and for pressure P throughout the domain for the three levels of mesh refinement. The maximum value of shear rate occurs at the singular die exit point and doubles from coarse to fine mesh solutions. The maximum value of P represents the pressure drop across the flow and is fairly stable around 6.75 units. Minimum values of P correspond to pressure pockets adjacent to the die exit within the jet flow.

Turning to comparison against analytical solutions, we consider flow profiles for velocity and pressure. The velocity profile for $x \leq 0$ (Figure 5(a)) shows a parabolic flow that gradually flattens. Similarly for $x \geq 0$, the velocity profile of Figure 5(b) reveals an initial flattened

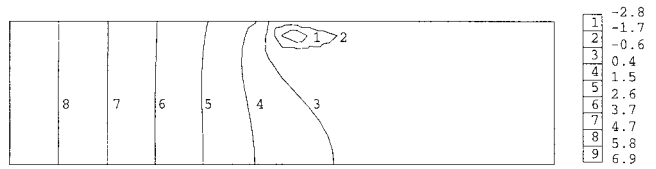

(a) pressure contours

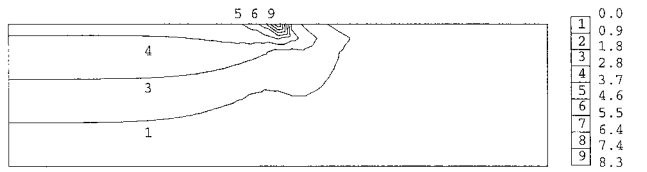

(b) I_2 contours

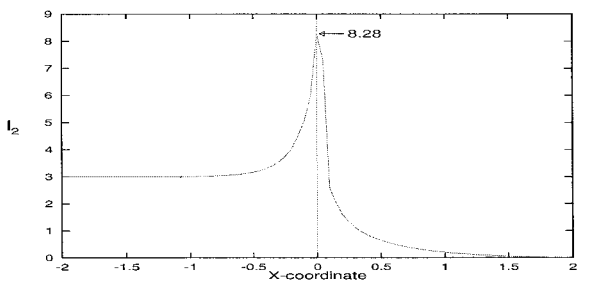

(c) I_2 on free surface

Figure 4. Planar stick–slip flow: medium mesh, $Re = 0$.

Table III. Shear rate and pressure for planar stick–slip flow: various meshes.

Solution		Course mesh	Medium mesh	Fine mesh
I_2	Max	5.86	8.28	10.14
P	Min	−1.35	−2.79	−3.91
	Max	6.76	6.89	6.75

parabolic form, which gradually adjusts to a linear pattern with increasing x. Table IV and Figure 6 provide tabular and graphical comparisons of velocity results with STGFEM scheme on coarse, medium and fine meshes, against the analytical solution of Richardson. The analytical solution for the streamwise velocity component V_x was derived from the streamfunction, as identified via the formula of Richardson [3] provided in Appendix A. Table V and Figure 7(a) provide equivalent data for pressure, where the Richardson solution has been reproduced based on the graphical information recorded in Reference [3]. The error in the

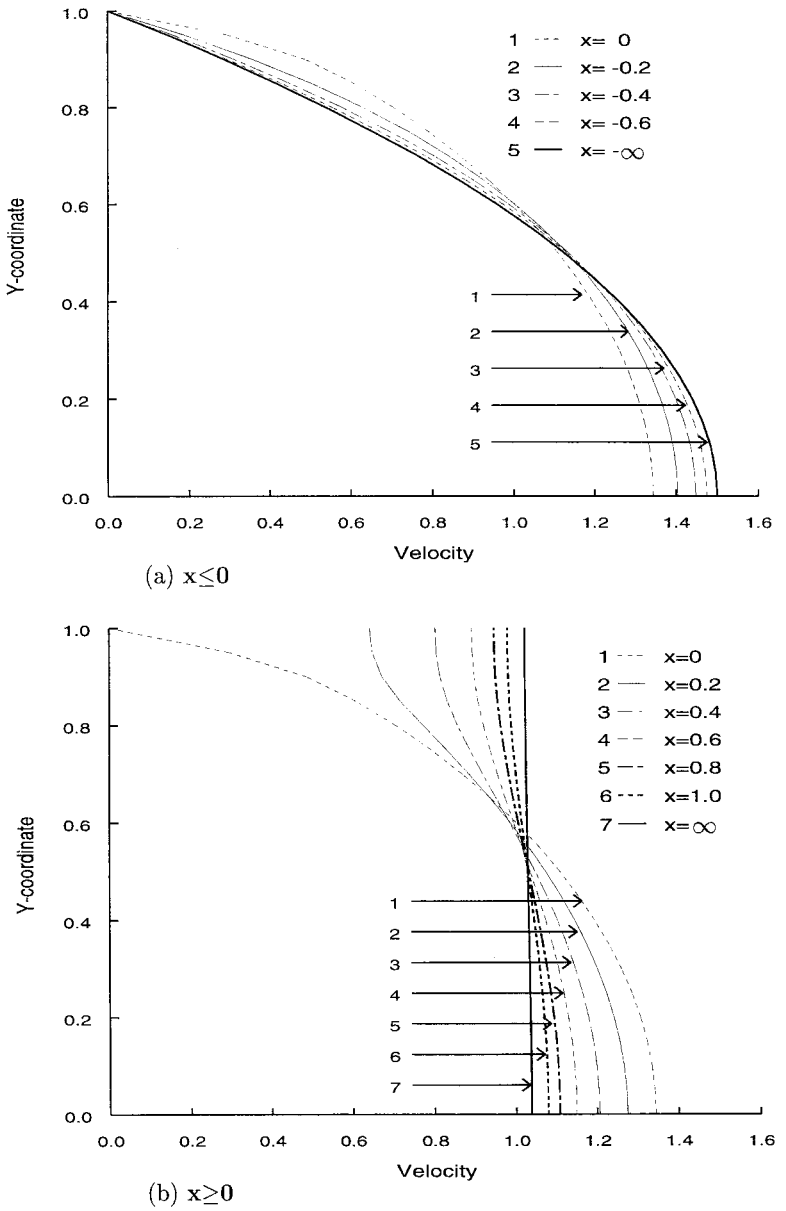

Figure 5. Planar stick–slip flow: medium mesh, cross–channel velocity profiles, $Re = 0$.

Table IV. Analytical and computed velocity along axis of symmetry: various meshes.

x axis	Richardson	Coarse mesh 200 elements	Medium mesh 800 elements	Fine mesh 1800 elements
−1.0	1.4964	1.4956	1.4958	1.4959
−0.8	1.4899	1.4889	1.4890	1.4892
−0.6	1.4758	1.4751	1.4747	1.4749
−0.4	1.4484	1.4496	1.4479	1.4479
−0.2	1.4027	1.4086	1.4042	1.4035
0.2	1.2798	1.2866	1.2737	1.2701
0.4	1.1967	1.2229	1.2059	1.2006
0.6	1.1308	1.1698	1.1494	1.1403
0.8	1.0834	1.1303	1.1074	1.0996
1.0	1.0516	1.1032	1.0787	1.0702

results decreases consistently and proportionally with refinement over coarse, medium and fine meshes.

Figure 7(a) shows the variation in pressure along the centreline in contrast to the Richardson analytical solution, and those on coarse, medium and fine meshes. All predictions show consistency and close correspondence for pressure to the analytical solution (see Table VI), decreasing linearly within the die, becoming more parabolic in shape in the jet region, as pressure tends to vanish. The corresponding results on accuracy for velocity and pressure are illustrated in Table VI with the comparison based on maximum error norm measures. The trend of behaviour for velocity with mesh refinement is displayed in Figure 7(c), which indicates $O(h^{1.9})$ inside and $O(h^{1.0})$ beyond the die. Hence, the velocity solution displays almost second-order accuracy in the die flow and first-order beyond. For the fine mesh results of Table VI, the error detected in velocity increases from 0.06 per cent within the die to 1.77 per cent beyond. For pressure, the error degradation is far less dramatic and the jet flow solution displays slightly less error than is the case for the die flow. Note the solution scaling in error norms for pressure is taken as unity for the jet flow as the size of the solution is less than unity. The error is 2.43 per cent within the die. Beyond the die the error is represented as 3.78 per cent.

In Table VII, the STGFEM velocity results (at $x = 0.2$ units on the free surface after the die exit) of the three mesh refinements are compared with the analytical solution of Richardson, the numerical SBEM results of Ingham and Kelmanson, and the SFEM and ISBFM results of Georgiou *et al.* (recorded to precision quoted in original references, correcting for the noted anomaly cited in Georgiou *et al.* [8] of Richardson's result). The STGFEM is found to be consistent across meshes, providing a convergent trend in velocity with mesh refinement. The velocity on the finest mesh lies between the analytical result of Reference [3] and the numerical results of References [5,8,9], falling within an error of about 3 per cent. The corresponding Figure 7(b) shows the velocity adjustment with increasing x near the die exit as the fluid travels away from the singularity ($x = 0$). This figure also compares the analytical solution with others from the literature. From this plot and the values of Table VII, we note for uniform meshing velocity agreement in trend along the top surface with Ingham *et al.* [5] and Georgiou *et al.* [8,9],

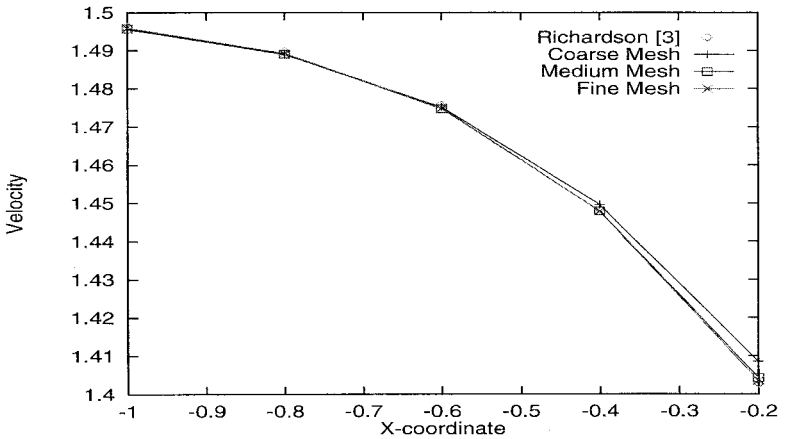

(a) $x<0$

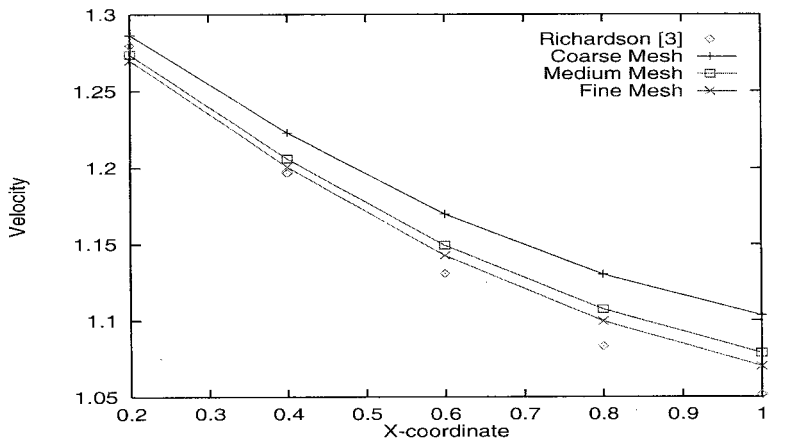

(b) $x>0$

Figure 6. Planar stick–slip flow: analytical and numerical solutions for velocity field along centreline $y = 0$, $Re = 0$.

though slightly overestimated in value. The departure from the analytical solution in the results of References [5,8,9] may be somewhat attributed to the overall uniformity in meshing they adopt. For the biased fine meshing option, there is an increased tendency towards the analytical solution of Richardson, which reflects the improvement to be had with such an approach. At $x = 0.2$, the difference from the Richardson solution drops to $O(0.1$ per cent).

Table V. Analytical and computed pressure along axis of symmetry: various meshes.

x axis	Richardson ± 0.0001	Coarse mesh 200 elements	Medium mesh 800 elements	Fine mesh 1800 elements
−1.6	5.7264	5.5620	5.5786	5.5924
−1.2	4.4627	4.3587	4.3750	4.3887
−0.8	3.2488	3.1542	3.1688	3.1818
−0.4	2.0299	1.9834	1.9923	2.0003
0.0	1.0348	0.9916	0.9924	0.9980
0.4	0.4179	0.3759	0.3781	0.3801
0.8	0.1393	0.1174	0.1203	0.1208
1.2	0.0398	0.0354	0.0353	0.0354
1.6	0.0149	0.0095	0.0094	0.0094
2.0	0.0000	0.0000	0.0000	0.0000

5.2. Axisymmetric stick–slip flow and stick–slip/drag flow

For both axisymmetric stick–slip flow (ASSF) and stick–slip/drag flow (SSDF), the fine mesh of Figure 8(a) is used. Comparisons between these two flows for values of shear rate I_2 and pressure P are evident in Table VIII at the same level of entry flow rate.

The velocity vector plot for stick–slip/drag flow is displayed in Figure 8(b), which reveals an initial annular flow adjusting rapidly at the pipe outlet to finally assume a plug flow. The radial and axial velocity line contour plots for both cases are virtually identical to the case of planar stick–slip flow and are not repeated for conciseness (see Table VIII for relevant quantities). Figure 8(c) shows the pressure line contour plot, for which the initial inlet maximum value of 4.02 units decreases in a linear fashion while approaching the singularity where a minimum pressure of -3.01 units is observed. The shear rate contours of Figure 8(d) increase in value at the top surface, reaching a peak shear rate of 6.3 units at the singular point after which the shear rate drops sharply to zero. This is due to the dependence of shear rate upon the velocity gradient, which increases sharply in the neighbourhood of the die exit location, specifically along the boundary streamline. The general trends of behaviour in velocity, pressure and shear rate are exposed more starkly by direct comparison between those for pure ASSF and those for SSDF.

The comments above are borne out by the line plots of Figure 9. A comparison of axial velocity V_z along the free top surface for the two flows, ASSF and SSDF, is shown in Figure 9(a). The final value of free-stream velocity is reduced by 21 per cent in the drag flow case, due to the influence of the moving wire on the deformation. Comparisons of pressure and I_2 for ASSF and SSDF in the axial direction are made in Figure 9(b) and (c) respectively. The change in pressure drop between these two flows of Figure 9(b) is 17.6 per cent, with an SSDF value of 4.02 units and an ASSF value of 4.88 units. Hence, drag flow imposition gives rise to a decline in the rate of pressure drop as one might expect. Patterns are similar to the planar stick–slip case of Figure 7(a). The shear rate profiles of Figure 9(c) follow the general form of Figure 4(c) for planar stick–slip flow. The behaviour of I_2 in the neighbourhood of the singularity is exposed; see also Table VIII and Figure 8(d). Here field patterns are similar in Figure 8(d) to those of Figure 4(b). The SSDF value of 6.28 units represents a reduction of 21

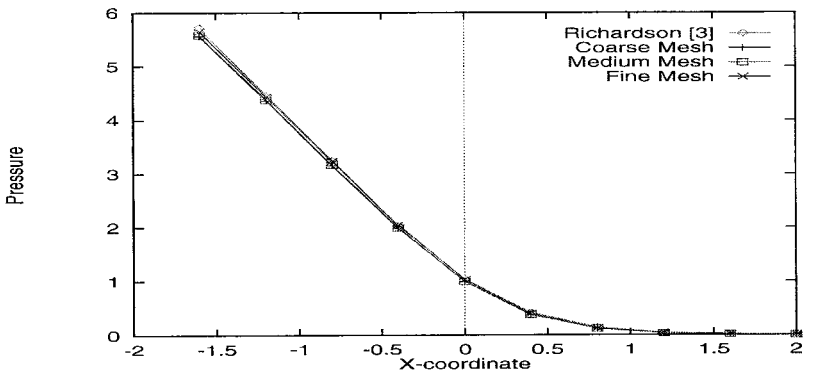

(a) pressure line plot along centreline y=0

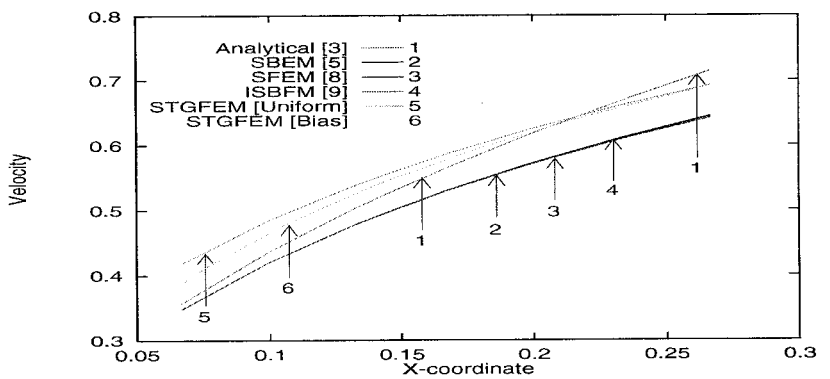

(b) velocity at free surface ($0.05 < x < 0.30$)

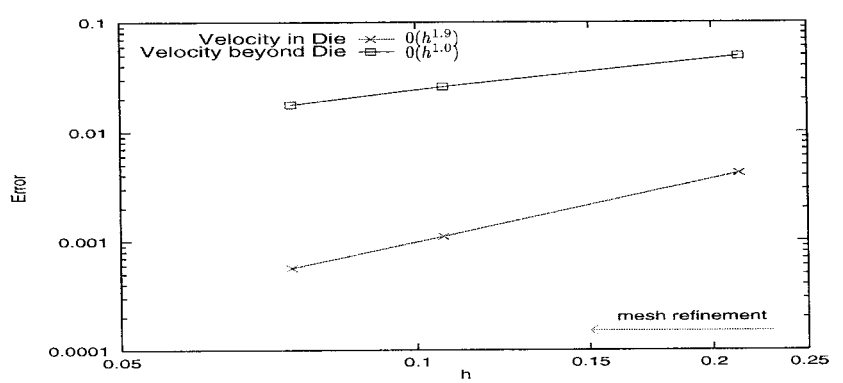

(c) velocity error norms against Richardson [3]

Figure 7. Planar stick–slip flow: analytical and numerical solutions, $Re = 0$.

Table VI. L_∞ error for velocity and pressure against analytical solution: various meshes.

L_∞ error	Coarse mesh $\Delta h = 0.20$	Medium mesh $\Delta h = 0.10$	Fine mesh $\Delta h = 0.07$
Velocity (in die)	0.004175	0.001102	0.000595
Velocity (beyond die)	0.049145	0.025848	0.017731
Pressure (in die)	0.028702	0.025803	0.023395
Pressure (beyond die)	0.041986	0.039850	0.037820

Table VII. Analytical and computed velocity results at $x = 0.2$ on free surface after die exit.

Method	Velocity
Analytical [3]	0.618040
SBEM [5]	0.572608
SFEM [8]	0.571896
ISBFM [9]	0.571259
STGFEM (coarse mesh)	0.690559
STGFEM (medium mesh)	0.643575
STGFEM (fine mesh)	0.625190
STGFEM (biased fine mesh)	0.619786

per cent from the ASSF value of 7.93 units. Clearly this is directly attributable to the additional drag flow component.

5.3. *Die-swell flow*

The vector velocity plot of Figure 11(a) shows an initial inlet Poiseuille flow that adjusts to a final plug flow. The radial velocity lines under die swell conditions (Figure 11(b)), reflect the stick–slip transition at the upper boundary. The contour plots of Figure 11(b)–(e) reflect close agreement with the findings of Nickell *et al.* [11], even taking into account the differences in meshing. The radial velocity increases towards the centre of this zone; the maximum value of 0.14 units occurring at the centre. Figure 11(c) illustrates contour lines for the axial velocity. It should be noted that V_z increases at the top boundary after the die exit, while on the symmetry axis it diminishes from an inlet value of unity to an exit free jet value of around 0.4 units (Figure 12(a)).

The shear rate (I_2) line contours of Figure 11(e) show a localized singularity, whose maximum is 10.75 units. In conjunction with Figure 12(c), we may discern that the shear rate at the top boundary initially commences from a constant value of 1.4 units, but increases exponentially upon nearing the singularity until it peaks at 10.75 units. The shear rate then drops rapidly with further increase in z, departing from the singularity ($z > 0$) to eventually vanish at approximately $z = 1.2$ units. The contour plot of pressure in Figure 11(d) indicates a maximum inlet value of 4.9 units and minimum value of -7.1 units at the singularity. Comparisons are made in Table IX for shear rate maxima I_2 and pressure P extrema, on the

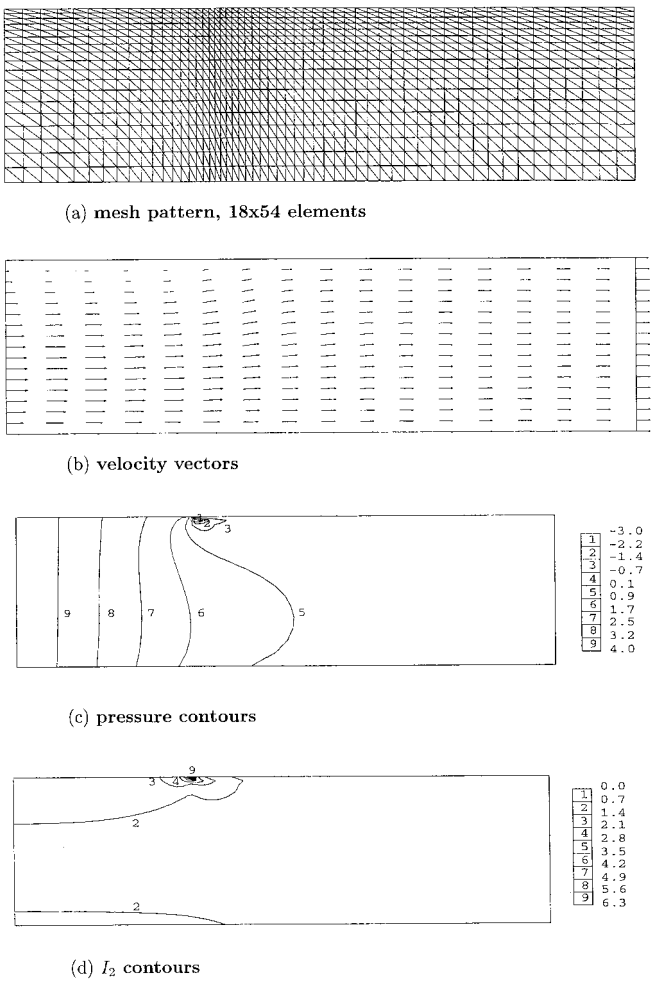

Figure 8. Stick–slip/drag flow: $Re = 10^{-4}$.

Table VIII. Axisymmetric stick–slip and stick–slip/drag flow: shear rate and pressure.

Solution		ASSF	SSDF
I_2	Max	7.93	6.28
P	Min	−3.92	−3.01
	Max	4.88	4.02

three levels of refinement and two different mesh structures. Since the adjustment between coarse and fine mesh results is minor in pressure and minuscule for velocity, plots in the axial direction are shown only for the fine mesh. From Table IX, the difference in I_2 with mesh refinement is observed to be relatively large in the neighbourhood of the singularity. This is strictly a local phenomenon. On comparing the shear rate profile elsewhere there is very little

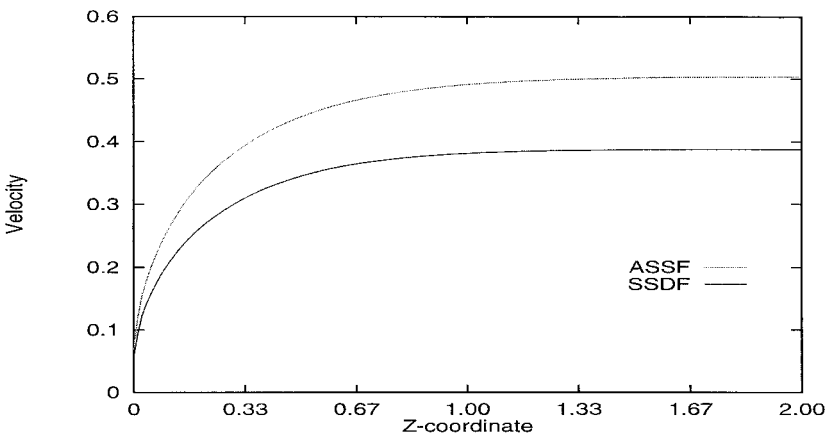

(a) V_z on free surface

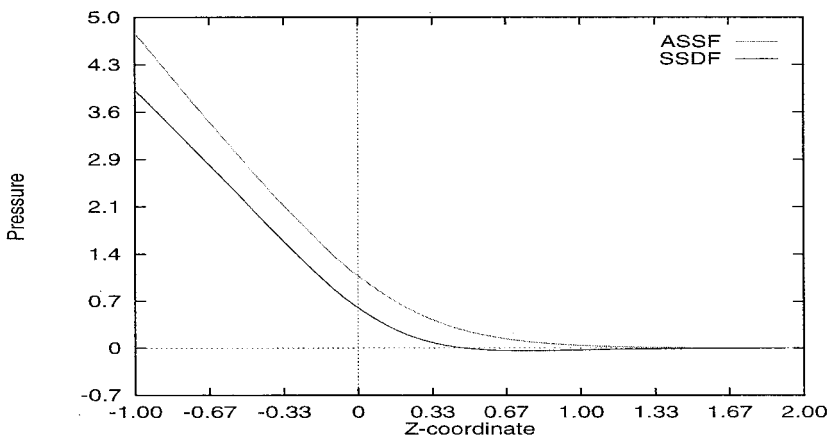

(b) pressure on axis of symmetry for stick-slip flow and inner surface for stick-slip/drag flow

Figure 9. Stick–slip flow and stick–slip/drag flow, $Re = 10^{-4}$.

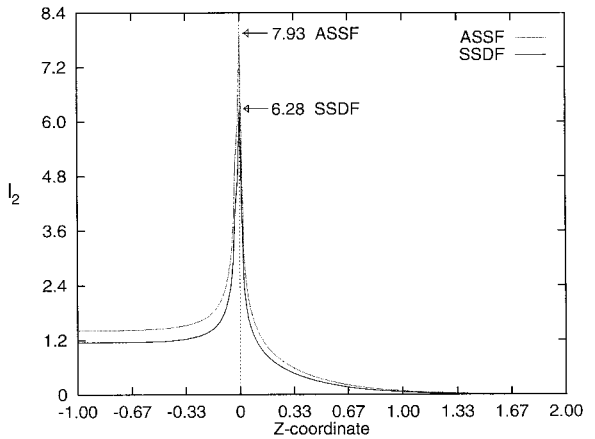

(c) I_2 on free surface

Figure 9 (*Continued*)

difference overall, amounting to 1 per cent at most between the coarse and fine meshes, with no observable difference between the medium and fine versions.

On comparing ASSF and die-swell flow for fine meshes in Figure 12, I_2 and pressure profiles are very similar within the die due to the imposition of equivalent inlet flow rates for both flows. The shear rate extrema at the singularity achieve maxima of 10.75 units for die-swell flow and 7.93 units for ASSF, representing an increase of 36 per cent (Figure 12(c)). Since for both cases with the fine UD mesh, stick–slip conditions apply before the die exit and entry flow lengths are identical, there is consequently little difference between pressure drop values over the die (0.01 per cent). On exit from the die, the effect of the die-swell on the free surface results in a slight drop in pressure. This is entirely in keeping with our prior results for planar stick–slip flow of Figure 7(a), where declining rates were contrasted against analytical values. Under the same imposed inlet flow rate, the difference in the velocity on the free surface between axisymmetric stick–slip flow and die-swell flow is displayed in Figure 12(a). The free-stream jet exit velocity is 21 per cent lower for die swell flow than for stick slip flow. Hence, as anticipated, we confirm that allowing the free surface to swell significantly reduces the flow speed to compensate.

Figure 13(a) provides the comparison of the derived die swell surfaces for the six different meshes. The corresponding values for swelling ratio are provided in Table X, where a direct comparison with results from the literature is performed. Figure 13(b) shows the effect of mesh refinement on L_∞ error for diagonal orientation meshes DU and UD for values see Table XI. With mesh refinement, maximum values of L_∞ errors for mesh UD and DU are $O(h^{1.6})$ and $O(h^{1.3})$ respectively. The swelling ratio is found to depend on the size of the smallest element and the orientation of the elements. The DU orientation gives approximately 50 per cent larger L_∞ error than the UD orientation (see Table XI), affecting swelling ratio results accordingly. This superior UD mesh performance (approaching second-order) is attributed to the richer

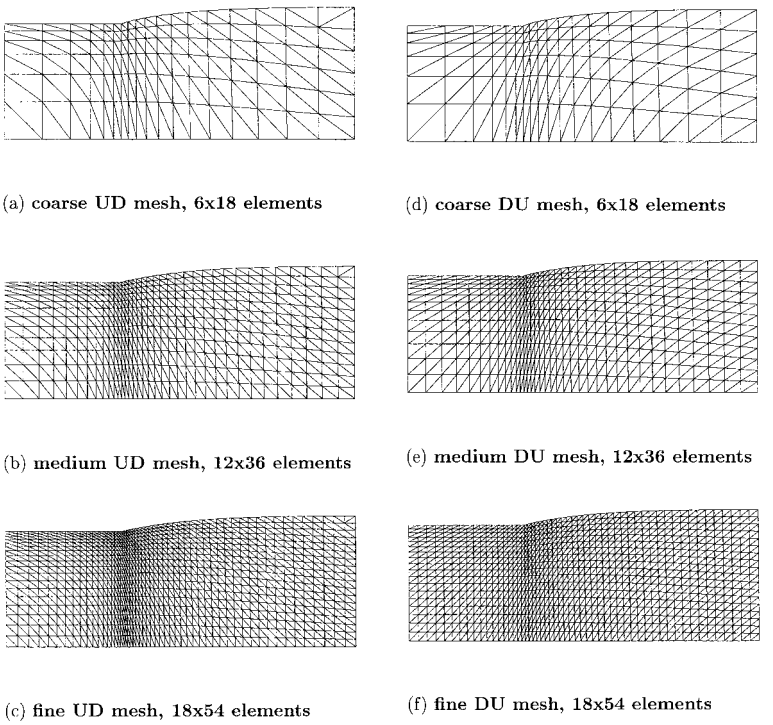

Figure 10. Die-swell flow: mesh patterns.

interpolation offered by the UD orientation for such quantities as velocity gradients. Those are represented in a discontinuous sense via the variational treatment (note also the connection to locking-corner meshing for primary variables). This we believe pervades many of the solutions reported in the literature, wherever continuous interpolation for primary variables is adopted. Rectangular meshing would suffer from these drawbacks in a likewise manner, being even more restrictive in the variation of functionality offered around the singular point. From Table X, we find that the swelling ratio of the medium refinement meshes, UD and DU is close to that of Tanner [10], the error being 0.2 per cent for the UD mesh. The swelling ratio of the fine UD mesh is the closest estimate to that of Nickell *et al.* [11] with an error of 0.3 per cent in that case. Tanner also provides an asymptotic estimate of $\chi = 1.130$. This correspondence with the literature may be taken as a strong indication of acceptable accuracy in our results. As indicated above, the orientation of the diagonal element in the mesh that intersects with the singularity, is an important factor and influences the accuracy of the corresponding solutions. To demonstrate this issue, the error in the swelling ratio is charted in Table XI against Nickell *et al.* results, on the two DU and UD mesh sets. Trends in convergence are superior for the UD mesh sets in comparison with those for DU. A hybrid fine mesh strategy also

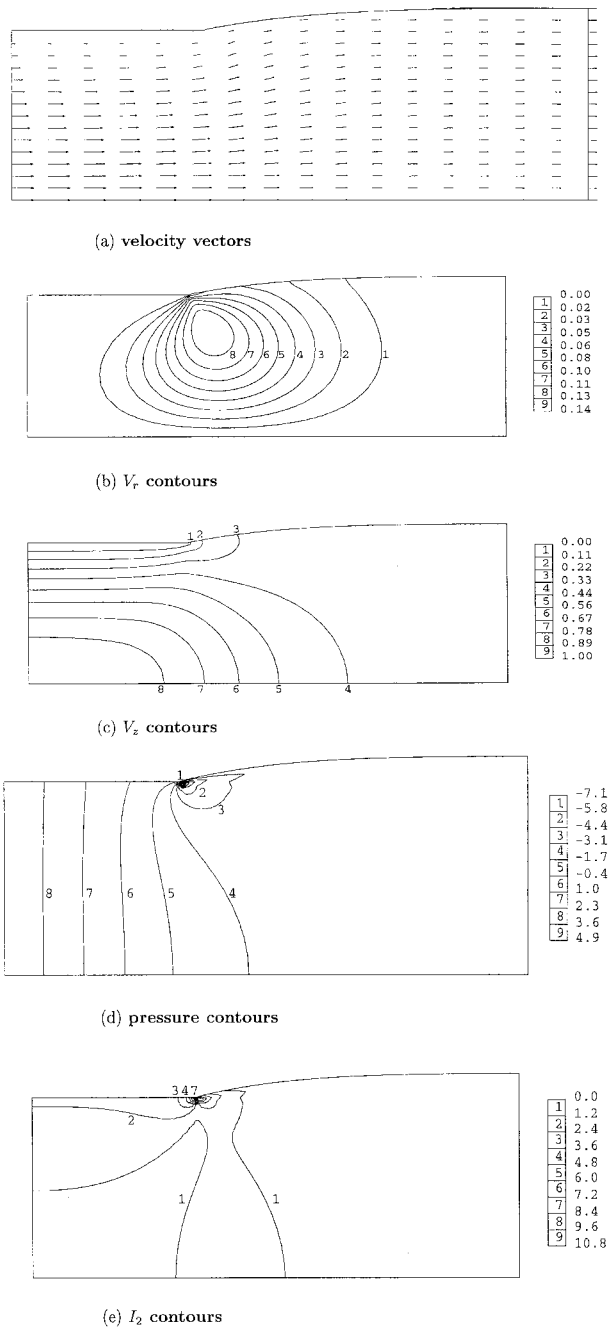

Figure 11. Die-swell flow: fine UD mesh, $Re = 10^{-4}$.

implemented, of DU in the die (Figure 10(f)) and UD in the jet (Figure 10(c)), gave a marginal improvement over the UD option in swelling ratio to reach the asymptotic value of $\chi = 1.30$. It is also noted that the separation angle θ between the horizontal and the exterior swelling edge of the first element after the singular point is smaller for the UD meshes. This angle tends to a value of 17.5° with mesh refinement on the UD meshes, as compared with 20.8° for the DU alternative.

In contrast, on testing the Phan-Thien free surface procedure, correspondingly larger swelling ratios are derived. It has been found necessary to impose an additional velocity free

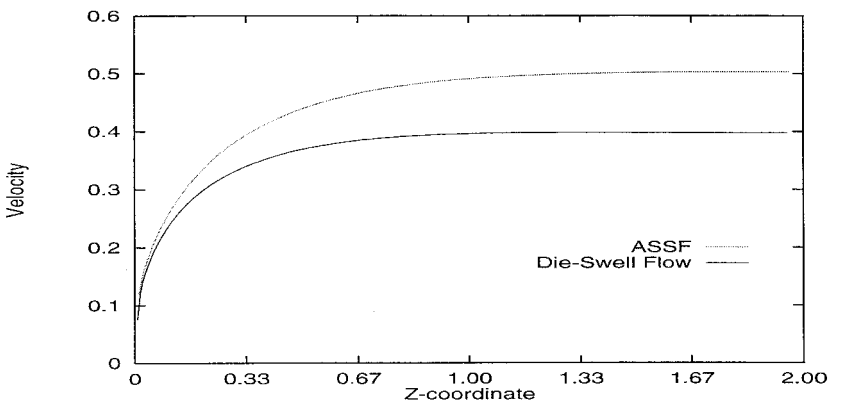

(a) V_z on free surface

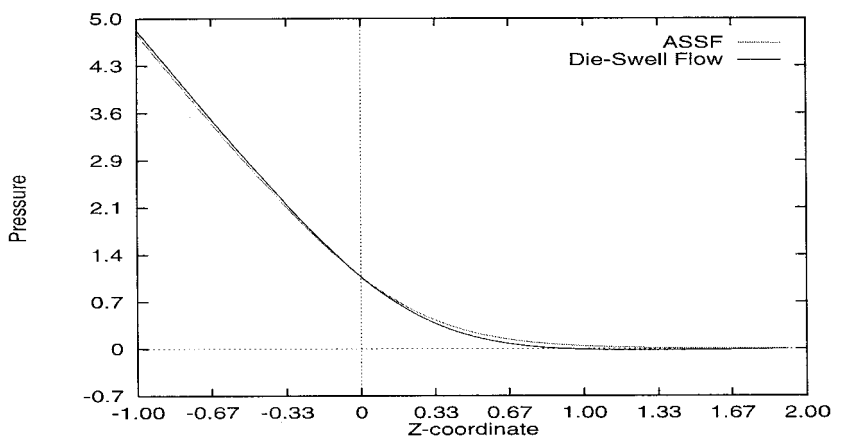

(b) pressure on axis of symmetry for stick-slip flow and die-swell flow

Figure 12. Stick–slip flow and die-swell flow, fine UD mesh, $Re = 10^{-4}$.

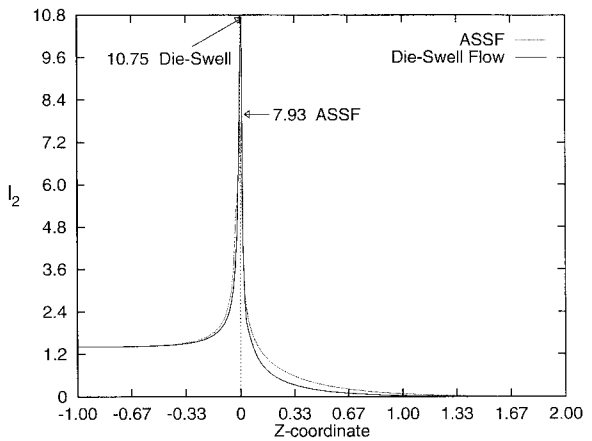

(c) I_2 on free surface

Figure 12 (*Continued*)

Table IX. Die-swell flow: shear rate and pressure.

Solution		C mesh UD	M mesh UD	F mesh UD	C mesh DU	M mesh DU	F mesh DU
I_2	Max	5.36	8.33	10.75	6.24	9.67	12.16
P	Min	−3.06	−5.32	−7.10	−2.62	−4.90	−6.43
	Max	4.96	4.94	4.94	4.97	4.96	4.96

surface boundary correction with this procedure to ensure tangential conditions and vanishing shear stress. Without such a correction, the results on swell and angle are considerably inaccurate. Table XII displays swelling ratio and angle computed on coarse and fine UD meshes. The corresponding swelling ratios are 35.4 and 35.0 per cent respectively, with separation angles of 23.7° for the coarse and 23.6° for the fine mesh. Both of these estimates are marked in their departure from the results of Nickell *et al.* and other investigators. For example, on the mesh the error in swelling ratio from that of Nickell *et al.* is 19.7 per cent. Hence, for current purposes, and as implemented here in a pointwise fashion following the original author, this method is discarded on the grounds of inaccuracy.

5.4. Die-swell/drag flow

For this final flow instance under consideration, we allot for mesh (c) of Table II and Figure 10(c), as the swelling ratio errors on UD meshes are considerably lower than those for the DU meshes. A principal point of interest is to analyse the effect of the additional component of drag flow upon the undisturbed die-swell flow. In this regard, comparison is made in Table XIII for shear rate I_2 maxima and observed extrema for pressure P. For die-swell/drag flow,

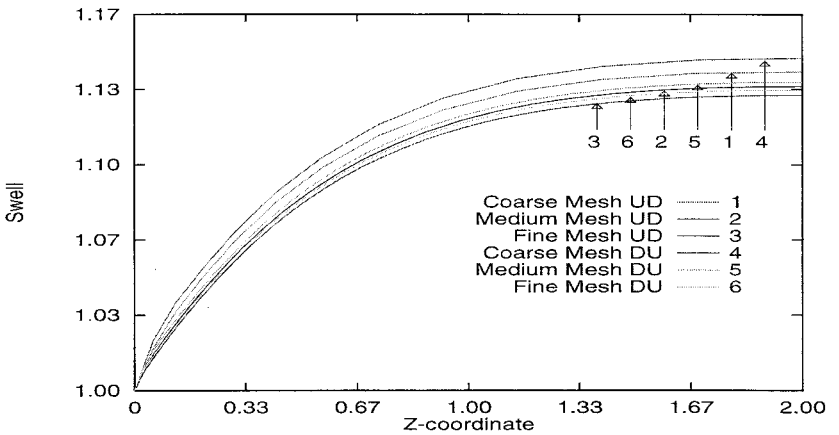

(a) swell free surface with mesh refinement

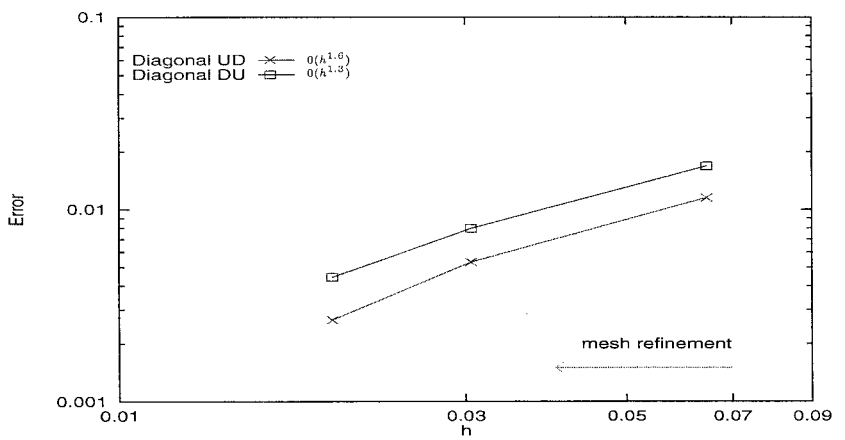

(b) die-swell error norms against Nickell et al. [11]

Figure 13. Die-swell flow: comparison of solutions, $Re = 10^{-4}$.

shear rate I_2 and pressure drop are reduced when compared with die-swell flow by 21 and 19.6 per cent respectively. The contours of Figure 14 bear this out. For Figure 14(a), in contrast to Figure 11(d), the pressure contours reflect the reduced effect on the negative pressure pockets (-5.58 units) near the singularity over the die-swell case (-7.1 units). Likewise, values of shear rate maxima alter from Figure 14(b) (8.47 units) to that for die-swell in Figure 11(e) (10.75 units).

Table X. Swelling ratio for die-swell flow.

Investigator	χ	χ (per cent)
Tanner [10]	1.136	13.6
Nickell *et al.* [11]	1.128	12.8
Chang *et al.* [12]	1.139	13.9
Crochet and Keunings [13]	1.126	12.6
Coarse UD mesh	1.141	14.1
Medium UD mesh	1.134	13.4
Fine UD mesh	1.131	13.1
Coarse DU mesh	1.147	14.7
Medium DU mesh	1.137	13.7
Fine DU mesh	1.133	13.3
Fine DU-UD mesh	1.130	13.0

Table XI. Swelling ratio error for UD and DU meshes against Nickell *et al.* [11] results.

Mesh	L_∞ error $* 10^{-2}$	θ (degree)	$\Delta h * 10^{-2}$
(a) Coarse UD mesh	1.1525	18.2881	6.4550
(b) Medium UD mesh	0.5319	17.8016	3.0533
(c) Fine UD mesh	0.2660	17.5737	1.9667
(d) Coarse DU mesh	1.6944	21.4798	6.4550
(e) Medium DU mesh	0.7979	20.9369	3.0533
(f) Fine DU mesh	0.4433	20.4761	1.9667
(g) Fine DU-UD mesh	0.1525	17.6604	1.9667

Table XII. Swelling ratio and angle for Phan-Thien strategy.

Mesh	χ	θ (degree)
Coarse UD mesh	1.354	23.6660
Fine UD mesh	1.350	23.6121

Table XIII. Die-swell flow and die-swell/drag flow:shear rate and pressure.

Solution		Die-swell flow	Die-swell/drag flow
I_2	Max	10.75	8.47
P	Min	−7.10	−5.58
	Max	4.94	3.97

The finer and more localized detail comparing these two flow scenarios is extracted in the line plots of Figure 15. Figure 15(c) illustrates the pressure P on the inner surface and Figure 15(d) the shear rate (I_2) at the free surface. The line pressure plot reveals that drag flow gives

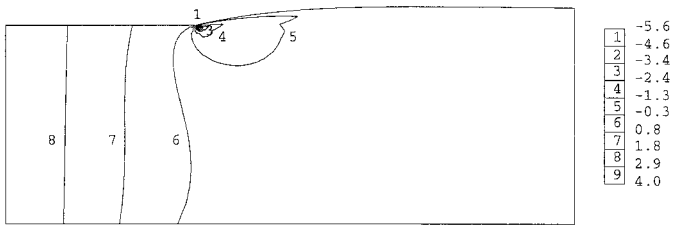

(a) pressure contours

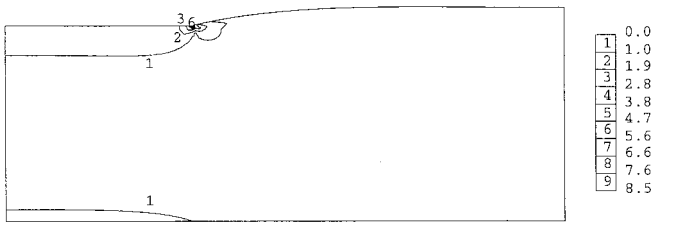

(b) I_2 contours

Figure 14. Die-swell/drag flow: fine UD mesh, $Re = 10^{-4}$.

rise to a negative dip in pressure on the inner surface beyond the die exit. This was not present when drag flow was introduced for stick–slip flows (see Figure 9(b)), and so is a consequence of the die-swell setting. Also, the decline in pressure drop is prominent. The shear rate profile of Figure 15(d) (Table XIII) can be compared against both Figure 9(c), for ASSF–SSDF (Table VIII), and Figure 12(c) for ASSF–die-swell. In the die-swell setting, drag flow incurs a reduction in peak I_2 values (10.75–8.47 units), comparable with the effect noted for stick–slip (7.93–6.28 units). Alternatively, in the contrast between die-swell and stick–slip (with or without drag flow) there is a consistent trend in elevation of peak I_2 values once swelling is present (here by 35 per cent).

The radial and axial velocity contour plot for the die-swell/drag flow are similar in appearance to Figure 11(b) and (c), and are not reproduced for the sake of conciseness. Figure 15(a) and (b) provides line plot comparisons between die-swell flow and die-swell/drag flow for velocity and die-swell respectively at the free surface employing the fine UD mesh. At the outlet the free-stream velocity of die-swell/drag flow is reduced by 21 per cent over that of pure die swell, so that swelling reduces accordingly by 4.2 per cent. This is in keeping with the correspondence in flow rate at the outlet and our findings for the stick–slip scenario. The separation angle for die swell/drag flow is 17.19°, which is a reduction of 2.2 per cent on the former die swell case. This accounts for the above quoted reduction in swelling ratios between these two flow instances.

6. CONCLUSIONS

This study has provided an analysis of a Taylor–Galerkin/pressure–correction method in its application for model free surface flow problems. First, through the investigation of stick–slip flow we have been able to establish comparison against analytical and other numerical solutions, for which we find agreement to within order 1 per cent.

For die–swell flows, with the added complication of *a priori* unknown free surface location we find close correspondence on swelling ratio to that reported in the literature, to within

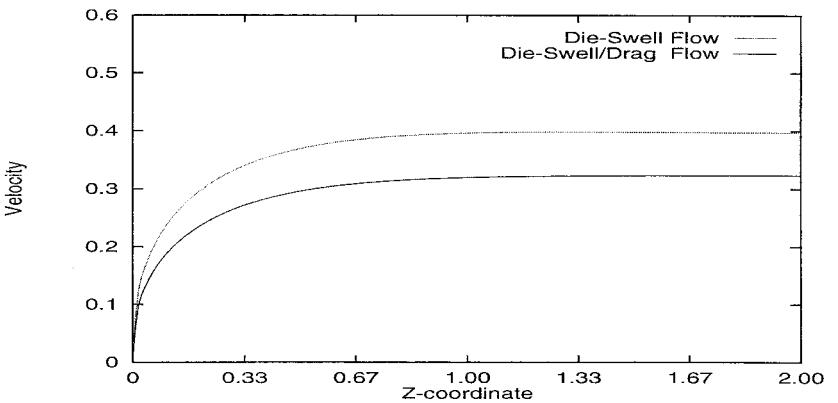

(a) **velocity**

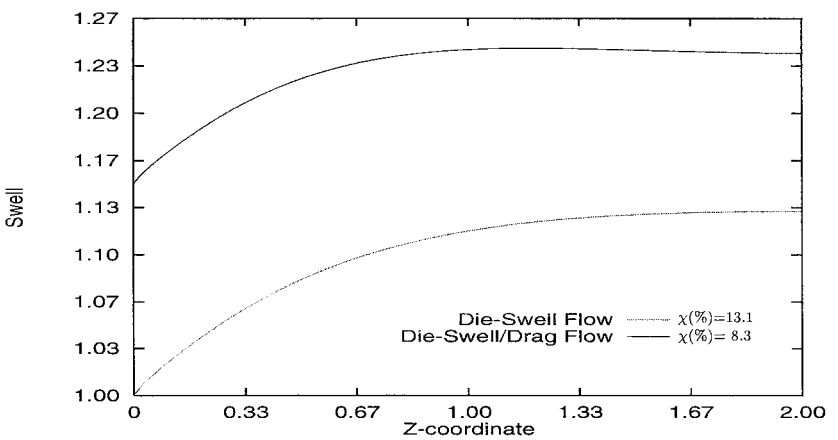

(b) **die swell**

Figure 15. Die swell flow and die-swell/drag flow, fine UD mesh.

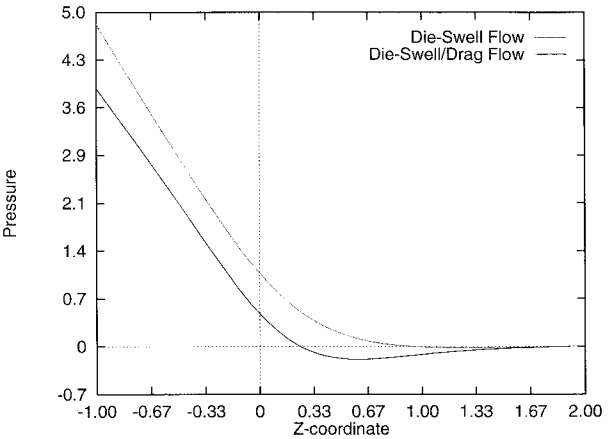

(c) pressure on axis of symmetry for die-swell flow and inner surface for die-swell/drag flow

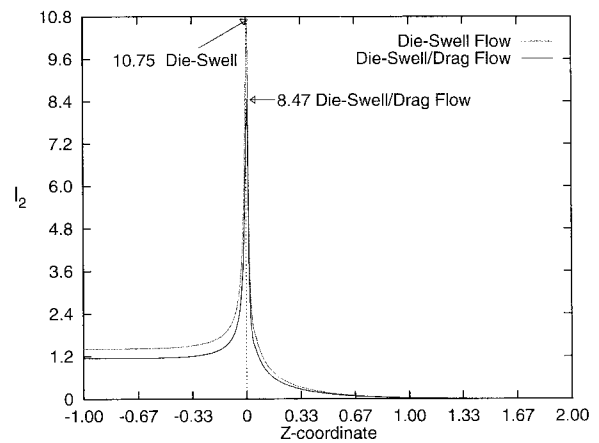

(d) I_2 on free surface

Figure 15 (*Continued*)

order 0.1 per cent. Through a careful study of mesh structure, we have also found that the accuracy of the solutions generated is sensitive to the orientation of the mesh in the location of the die exit. Here we have demonstrated that a poor selection of meshing may affect accuracy by up to 50 per cent. Accuracy has been demonstrated to pertain to second-order, with or without involvement of free surface location. This is so even in the presence of a die exit singularity to the flow in question.

In the comparison of stick–slip to die-swell flows under equivalent imposed inlet flow rate, the free-stream jet velocity is 21 per cent lower for die-swell flow than for stick–slip flow while pressure profiles barely differ. The shear rate extrema at the singularity peak at 10.75 units for die-swell flow, but attain the lower value of 7.93 units for stick–slip flow. Hence, shear rate extrema are elevated by 35 per cent once die-swell is incorporated.

We have also addressed the issue of associating an additional drag flow component to these two base type flows. This has afforded the opportunity to compare scenarios both with and without drag flow. Our findings reveal that shear rates at the singularity are reduced by as much as 21 per cent with the addition of drag flow for both slick–slip and die-swell flows. It is conspicuous that the same level of reduction in shear rate is observed for both flows. This we attribute to the local influence at the singularity that the inclusion of drag flow has. Likewise, pressure drops are also found to decrease by 17.6 per cent for stick–slip and 19.6 per cent for die-swell flow. In the die swell instance alone, the swelling ratio is observed to reduce by 4.2 per cent upon the addition of drag flow.

This research study may be viewed as a stepping stone towards the solution of more complex industrial based flows that involve coatings of one form or another. This is typically the case for example in processes such as wire coating, roller-coating and printing.

APPENDIX A

To derive the annular inlet flow profile, we follow Bird [23] and use the non-dimensional equation for annular pressure driven flow

$$V_z(r) = \frac{Pb^2}{4\mu L}\left\{1 - \left(\frac{r}{b}\right)^2 + \frac{1}{\ln(a/b)}\left[\left(\frac{a}{b}\right)^2 - 1 + \frac{4\mu L V_{\text{wire}}}{Pb^2}\right]\ln\left(\frac{a}{b}\right)\right\} \tag{A.1}$$

where variables are defined as viscosity μ, length Z_1Z_2 (Figure 1(b)) L, pressure drop between inlet and outlet P, wire speed V_{wire}, inner annular radius a and outer radius b.

Subsequently, we may derive the flow rate at inlet and relate this to pressure drop, via

$$Q = 2\pi \int_a^b r V_z(r)\, \mathrm{d}r \tag{A.2}$$

Hence, once flow rate Q is prescribed (say from an outlet plug or free jet flow), we may evaluate the pressure drop from the constant term, $Pb^2/4\mu L$, utilizing Equation (A.1) for $V_z(r)$ within Equation (A.2).

We have recourse to the streamfunction solution for planar stick–slip flow, as developed in the article of Richardson [3]

Case $x > 0$

$$\psi(x, y) = y - \frac{3}{2\pi}\sum_{n=1}^{\infty}\frac{(-1)^n}{B_-(-\mathrm{i}nx)}\, x\, \mathrm{e}^{-n\pi x}\sin n\pi y + \frac{3}{2}\sum_{n=1}^{\infty}(-1)^n \underset{w \to -\mathrm{i}nx}{Lt}\left[\frac{\mathrm{d}}{\mathrm{d}w}\left\{\frac{\mathrm{i}}{w^2 B_-(w)}\right\}\right]\mathrm{e}^{-n\pi x}\sin n\pi y$$

Case $x < 0$

$$\psi(x, y) = \frac{1}{2} y(3 - y^2)y - 3 \sum_{n=1}^{\infty} \Re\left\{ \frac{B_+(\frac{1}{2}\alpha_n)}{\sinh^2(\frac{1}{2}\alpha_n)} \left[\frac{\sinh(\frac{1}{2}\alpha_n y)}{\sinh(\frac{1}{2}\alpha_n)} - \frac{y \cos(\frac{1}{2}\alpha_n y)}{\cosh(\frac{1}{2}\alpha_n)} \right] e^{-i(1/2\alpha_n x)} \right\}$$

where

$$B_+(w) = -\frac{1}{3} \prod_{n=1}^{\infty} \frac{[1 + (2w/\alpha_n)][1 - (2w/\bar{\alpha}_n)]}{[1 + (w/in\pi)]^2}$$

and

$$B_-(w) = \prod_{n=1}^{\infty} \frac{[1 - (2w/\alpha_n)][1 + (2w/\bar{\alpha}_n)]}{[1 - (w/in\pi)]^2}$$

$$\alpha_n \approx \ln 2\beta_n + \left(\beta_n - \frac{\ln 2\beta_n}{\beta_n} \right) i$$

and

$$\beta_n = 2n\pi + \frac{1}{2}\pi, \quad n = 1, 2, 3, \ldots$$

To analyse accuracy in terms of mesh size, we may express the finite element solution for velocity as a power series expansion about the analytical solution

$$U^{Fe}(\Delta h) = U^{Anal} + C(\Delta h)^{\alpha}$$

This allows us to consider a L_∞ relative error measure for velocity against the analytical solution of Richardson on various meshes, each denoted by element size Δh

$$\frac{\max|U^{Anal} - U^{Fe}|}{\max|U^{Anal}|}$$

Here, variables are defined as the numerical solution U^{Fe}, the analytical solution U^{Anal}, size of the smallest element Δh, constant C, and the order of error constant α.

REFERENCES

1. Baloch A, Townsend P, Webster MF. On two- and three-dimensional expansion flows. *Computers and Fluids* 1995; **24**(8): 863–882.
2. Rameshwaran P, Townsend P, Webster MF. Simulation of particle setting in rotating and non-rotating flow of non-Newtonian fluids. *International Journal for Numerical Methods in Fluids* 1998; **26**: 851–874.
3. Richardson S. A 'stick-slip' problem relative to the motion of a free jet at low Reynolds numbers. *Proceedings of the Cambridge Philosophical Society* 1970; **67**: 477–489.

4. Okabe M. Fundamental theory of the semi-radial singularity mapping with applications to fracture mechanics. *Computational Methods in Applied Mechanics and Engineering* 1981; **26**: 53–73.
5. Ingham DB, Kelmanson MA. *Boundary Integral Equation Analyses of Singular Potential and Biharmonic Problems*. Springer: Berlin, 1984; 21–51.
6. Kermode M, Mckerrell A, Delves LM. The calculation of singular coefficients. *Computational Methods in Applied Mechanics and Engineering* 1985; **50**: 205–215.
7. Cuvelier C, Segal A, van Steenhoven AA. *Finite Element Methods and Navier–Stokes Equations*. D. Reidel: Dordrecht, 1986.
8. Georgiou GC, Olson LG, Schultz WW, Sagan S. A singular finite element for Stokes flow: the stick–slip problem. *International Journal for Numerical Methods in Fluids* 1989; **9**: 1353–1367.
9. Georgiou G, Olson L, Schultz W. The integrated singular basis function method for the stick–slip and the die-swell problem. *International Journal for Numerical Methods in Fluids* 1991; **13**: 1251–1265.
10. Tanner RI. *Engineering Rheology*. Oxford University Press: London, 1985.
11. Nickell RE, Tanner RI, Caswell B. The solution of viscous incompressible jet and free surface flows using finite-element methods. *Journal on Fluid Mechanics* 1974; **65**(1): 189–206.
12. Chang PW, Patten TW, Finlayson BA. Collocation and Galerkin finite element methods for viscoelastic fluid flow—II. *Computers and Fluids* 1979; **17**: 285–293.
13. Crochet MJ, Keunings R. Die swell of a Maxwell fluid numerical prediction. *Journal of Non-Newtonian Fluid Mechanics* 1980; **7**: 199–212.
14. Crochet MJ, Keunings R. On numerical die swell calculation. *Journal of Non-Newtonian Fluid Mechanics* 1982; **10**: 85–94.
15. Silliman WJ, Scriven LE. Separating flow near a static contact line: slip at a wall and shape of a free surface. *Journal of Computational Physics* 1980; **34**: 287–313.
16. Ngamaramvaranggul V, Webster MF. Simulation of coating flows with slip effects. *International Journal for Numerical Methods in Fluids* 2000; **33**: 961–992.
17. Phan-Thien N. Influence of wall slip on extrudate swell: a boundary element investigation. *Journal of Non-Newtonian Fluid Mechanics* 1988; **26**: 327–340.
18. Bevarly CR, Tanner RI. Numerical analysis of three-dimensional Newtonian extrudate swell. *Rheology Acta* 1991; **30**: 341–356.
19. Karagiannis A, Hrymak AN, Vlachopoulos J. Three-dimensional non-isothermal extrusion flows. *Rheology Acta* 1989; **28**: 121–133.
20. Butler CW, Bush MB. Extrudate swell in some dilute elastic solution. *Rheology Acta* 1989; **28**: 294–301.
21. Ahmed R, Liang RF, Mackley MR. The experimental observation adn numerical prediction of planar entry flow and die swell for molten polyethylenes. *Journal of Non-Newtonian Fluid Mechanics* 1995; **59**: 129–153.
22. Crochet MJ, Davies AR, Walters K. *Numerical Simulation of Non-Newtonian Flow*. *Rheology Series 1*. Elsevier Science: Amsterdam, 1984.
23. Bird RB, Steward WE, Lightfoot EN. *Transport Phenomena*. Wiley: New York, 1960.

